MOdel-based SyntheTic Data-driven Learning (MOST-DL): Application in Single-shot T$_2$ Mapping with Severe Head Motion Using Overlapping-echo Acquisition

Qinqin Yang, Yanhong Lin, Jiechao Wang, Jianfeng Bao, Xiaoyin Wang, Lingceng Ma, Zihan Zhou,
Qizhi Yang, Shuhui Cai, Hongjian He, Congbo Cai, Jiyang Dong, Jingliang Cheng,
Zhong Chen, Jianhui Zhong

Abstract—Data-driven learning algorithms have been successfully applied to facilitate reconstruction of medical imaging. However, real-world data needed for supervised learning are typically unavailable or insufficient, especially in the field of magnetic resonance imaging (MRI). Use of synthetic training samples has provided a potential solution for such problems, while the challenges brought by various non-ideal situations were usually encountered, especially under complex experimental conditions. In this study, a general framework, MOdel-based SyntheTic Data-driven Learning (MOST-DL), was proposed to generate pairing data from the first principle to address the lack of labeling in supervised learning scenarios. A challenging application is demonstrated to verify the proposed framework and achieve robust T$_2$ mapping using overlapping-echo acquisition under severe head motion accompanied with inhomogeneous RF field. We decomposed the process into two main steps: (1) calibrationless parallel reconstruction and (2) end-to-end T$_2$ mapping with motion correction. The neural network was first trained in pure synthetic data and then evaluated with *in vivo* human brain without fine-turning. Both simulation and *in vivo* experiments showed that the MOST-DL method significantly reduces ghosting and motion artifacts in T$_2$ maps in the presence of random and continuous subject movement. The proposed approach may open a door for solving similar problems with other MRI acquisition methods and can be extended to other areas of medical imaging.

Index Terms—Synthetic data generation, Overlapping-echo acquisition, Motion correction, Single-shot T2 mapping, Calibrationless parallel reconstruction.

Qinqin Yang, Yanhong Lin, Jiechao Wang, Lingceng Ma, Qizhi Yang, Shuhui Cai, Zhong Chen, Congbo Cai and Jiyang Dong are with the Department of Electronic Science, Xiamen University, Xiamen, 361005, China.

Jianfeng Bao and Jingliang Cheng are with the Department of Magnetic Resonance Imaging, The First Affiliated Hospital of Zhengzhou University, Zhengzhou University, Zhengzhou, 450052, China.

Xiaoyin Wang, Zihan Zhou and Hongjian He are with the Center for Brain Imaging Science and Technology, College of Biomedical Engineering and Instrumental Science, Zhejiang University, Hangzhou, Zhejiang, 310027, China.

Jianhui Zhong is with the Department of Imaging Sciences, University of Rochester, Rochester, New York, USA.

I. INTRODUCTION

DATA, algorithms and computing power are the troika of modern artificial intelligence (AI) [1]. As the first step in AI-based medical imaging processing, many problems come down to insufficient or imperfect data, especially in magnetic resonance imaging (MRI) due to the significant economic burden and long acquisition time for data collection [2]. In the last decade, many AI-based methods have achieved excellent results in one or a few public datasets, but faced challenges in translating into broad clinical applications due to differences among various experimental instruments and situations. Collecting raw data in the field of medical imaging is relatively easy, while data labeling (e.g., informative annotations) is expertise-dependent and often prohibitively time-consuming. Furthermore, training labels may not be available for some complex situations, such as the difficulty of measuring quantitative physical parameters or the irreversibility of the behavior during data collection.

With the development of computer-aided simulation and high-quality rendering technology, synthetic data is increasingly used in AI systems [3]. In medical imaging, synthetic data has drawn significant attention and been used to address the lack of large datasets [4], and have provided powerful solutions in applications such as cardiac imaging [5]–[7] and nuclei segmentation in histopathologic images [8]. Among these, the data-driven (model-free) algorithms, especially generative adversarial networks (GANs), play a key role in generating realistic synthetic data. Learning in synthetic data could accelerate the rollout of data-driven learning algorithms through lower-cost and faster data collection. Furthermore, synthetic data can protect patient privacy, and enable greater reproducibility in research. Despite many advantages, data-driven synthesis methods are constrained by the size of the available training dataset, and the biased datasets may lead the trained model towards overrepresented conditions. Chen *et al.* [9] have expressed concerns about the proliferation of synthetic data created by data-driven methods and recommended the use of simulation-based synthetic data created from forward models [10] (e.g., existing clinical reference standards, medical prior knowledge and physical laws), which may have regulatory advantages and better interpretability.

Patient motion during MRI scan results in phase mismatch and image artifacts, which can degrade image quality, especially in quantitative MRI (qMRI). Recently, an increasing number of algorithms involving motion correction in qMRI were proposed, and most of them focus on multi-shot sequences [11]–[13]. Due to the irreversible nature of motion, the single-shot acquisition is in general more robust to subject motion (especially severe motion) compared with the multi-shot acquisition. Multiple overlapping-echo detachment (MOLED) sequence [14]–[16], proposed by our group, has been successfully applied in single-shot qMRI with high accuracy. In MOLED acquisition, overlapping-echo signals containing different phase evolution and relaxation weighting are encoded and collected in a single scan with echo planar imaging (EPI) readout. To reconstruct quantitative map from overlapping-echo signals, traditional numerical optimization method was initially used for signal separation but was subsequently replaced by end-to-end residual learning method based on convolutional neural network (CNN) [17]. However, the real paired dataset used for network training can only be acquired by different imaging sequences, which usually bring in different distortions, artifacts and signal-to-noise ratio (SNR), resulting in uncertainty in the mapping relationship.

To overcome the labeling challenges in supervised learning scenarios, we propose a general framework for synthetic data generation, termed MOdel-based SyntheTic Data-driven Learning (MOST-DL). We model the imaging process from the first principle and introduce a scheme to bridge the synthetic-to-real domain gap. With the help of MOST-DL, we focus on addressing a very challenging topic in MRI, i.e., achieving T_2 mapping under severe head motion for challenging subjects such as the elderly, children and patients suffering from stroke, emergency trauma, psychological disorders and epilepsy in clinical practice. The MOLED sequence is applied to acquire signals with different TE weighting at high efficiency, together with the parallel imaging technique to reduce image distortion. Therefore, the process can be separated into two independent tasks, i.e. (1) parallel reconstruction for ultra-fast pulse sequence and (2) end-to-end T_2 mapping with motion correction, both of which are suffer from difficulty in 'ground truth' acquisition.

II. RELATED WORKS

A. Parallel Reconstruction for Ultra-fast MRI

In the field of EPI/MOLED acquisition, parallel imaging is applied to reduce distortions from B_0 inhomogeneity and lessen T_2 blurring instead of acquisition acceleration [18], [19]. The autocalibration signal (ACS) used for interpolation kernel estimation is acquired prior to the under-sampled data, resulting in additional scan time and increased sensitivity to subject motion. Therefore, high-performance and robust calibrationless parallel reconstruction is increasingly becoming a vital factor in under-sampling EPI/MOLED acquisition.

Shin et al. [20] are one of the first to achieve calibrationless parallel imaging reconstruction. They proposed simultaneous autocalibrating and k-space estimation (SAKE) method, which formulates parallel reconstruction as low-rank matrix completion utilizing the redundancy from multi-coil k-space. Similarly, Lee et al. [21] proposed an annihilating filter-based low-rank Hankel matrix completion, termed ALOHA algorithm, to perform Nyquist ghost correction and parallel reconstruction in EPI acquisition. However, the low-rank matrix-based methods suffer from high computational costs and often fail to remove the artifacts in under-sampled EPI data due to the uniform Cartesian sampling [22]. Inspired by ALOHA algorithm, Lee et al. [23] further improved the result by using a deep neural network. Though the deep learning method has already achieved calibrationless reconstruction of EPI data, it still needs a large number of ALOHA reconstructed images as labels, which introduces additional reconstruction error in network training and is challenging in label producing as the author reported. To the best of our knowledge, we are the first to utilize synthetic data to address the labeling challenge in ultra-fast MRI reconstruction.

B. Deep Learning for MRI Motion Correction

Regarding motion correction in MRI, most existing deep learning approaches are based on motion simulation from real-world motion-free data [24]–[27]. Among the state-of-the-art methods, a representative method presented by Johnson et al. [26] performed motion simulation in motion-free MR images and combined different motion frames in a new k-space to generate motion-corrupted samples. In order to improve the simulation accuracy, Duffy et al. [27] performed motion simulation by phase shift and rotation in k-space with non-uniform fast Fourier transform (NUFFT). These works involve direct motion operation and interpolation in acquired MR images, which can be called retrospective motion simulation. However, the retrospective approaches still require a large number of real-world motion-free data using specific pulse sequences. They cannot simulate the effects caused by RF inhomogeneity and the effects caused by motion before the sampling stage (e.g., during diffusion or MOLED encoding).

Motion correction has always been studied as a separate step, which has a negative impact on qMRI [28]. Although single-shot MRI scan is robust to slight subject motion, some problems still occur under severe motion, especially in qMRI. Therefore, we combine the process of motion correction and relaxation parameter mapping to avoid the secondary propagation of error in a cascade framework.

C. Model-based Synthetic Data-driven Learning in MRI

Model-based synthetic data (MOST) generation relies on explicit forward physical models, which provides a more stable and interpretable strategy for data generation and network training. Quantitative MR parametric mapping is one of the most successful tasks where MOST has been applied, such as MR fingerprinting [29], [30] and chemical-exchange-saturation-transfer (CEST) imaging [31]. These works rely on fully connected networks for voxel-level fitting in synthetic data, but are heavily sensitive to noise. Some previous works proposed by Liu et al. [32], [33] also involve model-driven synthetic data in dynamic imaging and qMRI. They created discrete numerical phantoms covering various tissue types, and

assigned the same value of relaxation parameters to each type of tissue, which result in excessive smoothing and loss of detailed texture in final templates. Therefore, their synthetic data are only used to verify the proposed algorithms, and a large amount of real data are still required when transformed to the real world. Besides, the estimation and inversion of various electromagnetic parameters benefit from MOST methods, such as quantitative susceptibility mapping (QSM) [34], [35] and electrical properties tomography (EPT) [36]. These methods have achieved high performance in solving specific problems but are difficult to generalize to other applications.

Previously our group introduced MOST in MRI reconstruction based on general Bloch equation evolution. The synthetic data were used in training deep neural networks to achieve end-to-end T_2 mapping from MOLED/OLED images [15], [17] and distortion correction in gradient-echo EPI sequence [37]. However, the synthetic data was initially created by geometrical shapes such as ellipses, triangles and rectangles, which are quite different from anatomical textures and cause some degree of domain gap between synthetic and real images. Moreover, subject motion as a major clinical MRI issue was not considered in the modeling, which limited the generalizability of the initial version.

This paper builds on our previous works, and the contribution and novelty can be summarized as follows:

- We present a general framework for generating synthetic MRI data for deep neural network training. Unlike previous works [15], [17], [29]–[33], [35]–[37], rich anatomical texture priors from publicly available databases are used as parametric templates instead of geometrical shapes or numerical phantoms, which allows the generation of data closer to the real situation;
- Various non-ideal factors are considered in this framework. In particular, the subject motion is modeled at sub-voxel level during Bloch simulation. Moreover, non-ideal factors reconstruction is used as a quality control indicator for secondary validation of the reliability in data generation;
- We demonstrate the utility of the framework by building two sets of paired data for motion-robust T_2 mapping in the human brain. The synthetic data address calibrationless parallel reconstruction for ultra-fast pulse sequence and intra-shot motion correction in MRI. We present extensive validation of the proposed framework by testing on unseen real-world data and clinical patient data.

III. MODEL-BASED SYNTHETIC DATA-DRIVEN LEARNING

A. Problem Formulation

The MRI system can be thought of as a forward physical model $\boldsymbol{A}$ that acts on J tissue relaxation parameters a_j which result in measurements b in image domain. For example, a_j represent T_1, T_2 and proton density (PD) in qMRI. Therefore, the forward of a general imaging problem can be formulated as:

$$b = \boldsymbol{A}(a_j, \sigma_k) + \epsilon. \tag{1}$$

where σ_k denotes K non-ideal factors and ϵ is the noise in the measured data. The non-ideal factors, σ_k, consist of

field inhomogeneity (ΔB_0, B_1^+, B_1^-), unexpected motion, instrument imperfections and so on.

Typically, data-driven learning algorithm aims to perform an end-to-end mapping between source data b_s and target data b_t as:

$$\hat{b}_t = f(b_s; \theta_\Omega). \tag{2}$$

where, f is a learning-based model such as convolutional neural network (CNN), which depends on the trainable parameters θ of a policy Ω. To solve this domain transformation problem, we can optimize the function:

$$\hat{\theta} = \arg \min_\theta \mathbb{E}_{(b_s, b_t) \sim P(b)} L[f(b_s; \theta_\Omega) - b_t]. \tag{3}$$

where $P(b)$ denotes the distribution of measured training sets, and $L[\cdot]$ is the loss function. $\mathbb{E}_{(b_s, b_t) \sim P(b)}[\cdot]$ represents the expectation of loss function when training sample (b_s, b_t) is drawn from distribution $P(b)$. By incorporating of MRI physical operator (1) into Equation (3), the optimization can eliminate the dependency on paired samples, which forms self-supervised learning [33]. The optimization can now be formulated as follows:

$$\hat{\theta} = \arg \min_\theta \mathbb{E}_{a \sim P(a), \sigma \sim P(\sigma)}$$
$$L[f(\boldsymbol{A}_{input}(a_j, \sigma_k^{in}); \theta_\Omega) - \boldsymbol{A}_{label}(a_j, \sigma_k^{out})]. \tag{4}$$

here, $P(a)$ and $P(\sigma)$ denote the distribution of tissue relaxation parameters (parametric templates) and non-ideal factors, respectively, $\boldsymbol{A}_{input}$ and $\boldsymbol{A}_{label}$ are the forward models to generate source and target data with the corresponding non-ideal factors σ_k^{in} and σ_k^{out}. Ideally, we would like to apply a model trained on synthetic data to real data. To achieve this purpose, we need to introduce *domain randomization* [38], which is to make the distribution of synthetic data sufficiently wide and diverse to bridge domain gap between synthetic and real images. Based on this, we can further control the $P(a)$ and $P(\sigma)$ with I configurations $\xi_i \in \Xi$ that the optimization can be parameterized as:

$$\hat{\theta} = \arg \min_\theta \mathbb{E}_{\xi \sim \Xi} \mathbb{E}_{a \sim P_\xi(a), \sigma \sim P_\xi(\sigma)}$$
$$L[f(\boldsymbol{A}_{input}(a_j, \sigma_k^{in}); \theta_\Omega) - \boldsymbol{A}_{label}(a_j, \sigma_k^{out})]. \tag{5}$$

in which, the randomization parameter ξ_i is bounded as $\xi_i = [\xi_i^{low}, \xi_i^{high}]$ and uniformly sampled within the range. Hence, we aim to determine a reasonable range of randomization parameter and create the parameterized data distribution of parametric templates, $P_\xi(a)$, and non-ideal factors, $P_\xi(\sigma)$.

A schematic of the MOST-DL framework is shown in Fig. 1. Briefly, we first synthesize the parametric templates including M_0, T_2, etc, from multi-contrast images of public database (Section.III-B). Meanwhile, non-ideal factors are constructed based on physical priors (Section.III-C). Depending on the specific task requirements, the model-based simulation will generate input data and corresponding label data, respectively, with the specific MRI sequences (Section.III-D). During data generation, domain randomization is performed to make the synthetic domain sufficiently wide and make the model trained on synthetic data robust enough for realistic data. As such, the framework can generate paired datasets for various supervised
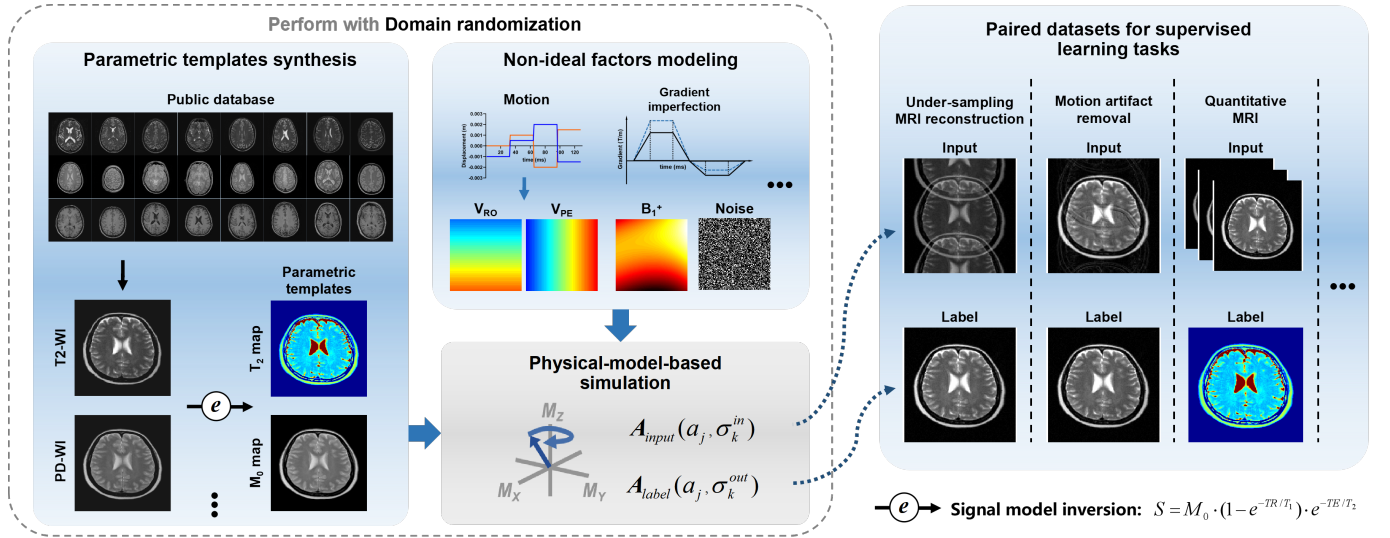
Fig. 1. Overview of the MOST-DL framework. Parametric templates synthesis: weighted images from public database are transformed to corresponding quantitative parametric maps (distribution $P_{\xi}(a)$) based on signal model. Non-ideal factors modeling: field inhomogeneity, unexpected motion, noise and instrument imperfections (distribution $P_{\xi}(\sigma)$) are generated by randomization. Physical-model-based simulation: paired datasets for supervised learning tasks are generated by Bloch simulation with task-specific pulse sequence, A_{input} and A_{label} are the forward models to generate source and target data.

learning tasks, such as under-sampling MRI reconstruction, motion artifact removal, qMRI, etc.

B. Parametric Templates Synthesis

The quantitative tissue parametric templates were synthesized from the realistic qualitative multi-contrast MR images by general MR signal model:

$$ S = M_0 \cdot (1 - e^{-TR/T_1}) \cdot e^{-TE/T_2} \tag{6} $$

Specifically, the PD-weighted image was first assigned as a 'virtual' M_0 map after intensity normalization under the conditions $TE \to 0$ and $TR \gg T_1$. To obtain the other parametric maps, the weighted images are used as S signal with the corresponding TE/TR value. The parameters distribution can be changed by adjusting the TE/TR value or intensity scaling.

In this work, the multi-contrast images used to produce parametric templates were from the public database IXI (https://brain-development.org/ixi-dataset/). It consists of five contrasts collected at three different hospitals in London. For IXI data, the matrix size is 256×256, and the imaging resolution is 0.94 mm × 0.94 mm × 1.25 mm. We randomly selected 200 subjects from Hammersmith Hospital and Guy's Hospital. The T_2-weighted volumes were selected as references for co-registration by elastix toolbox [39] based on Insight Segmentation and Registration Toolkit (ITK) with parameters "translation" and "affine". Two-dimensional (2D) slices were then sampled from the registered multi-contrast volumes and performed signal model inversion. The parametric templates were interpolated to a matrix size of 512×512 grids for high-accuracy simulation. Only slices covering the brain and cerebellum were considered and about 30 slices were extracted from each subject. Finally, a total of about 6000 slices were used for further model-based simulation.

C. Non-ideal Factors Modeling

1) Motion: The sub-voxel motion of each voxel under Bloch simulation is considered in this framework. A coordinate vector $s_0 = [x_0, y_0]$ of parametric templates is created and used to record the accurate position of echo spin (corresponding to the element of template matrix) at the different moment during motion. The additional phase accumulation for each spin at arbitrary evolution time t can be represented as an integral of additional precession frequency caused by motion:

$$ \Delta\varphi(x,y,t) = \gamma \int_0^t [G_{RO}(\hat{t}) \cdot (x_{\hat{t}} - x) + G_{PE}(\hat{t}) \cdot (y_{\hat{t}} - y)]d\hat{t} \tag{7} $$

where γ is the gyromagnetic ratio, $G_{RO}(t)$ and $G_{PE}(t)$ are the time-varying linear gradient field along the frequency and phase encoding directions, respectively. Hence, all spins with additional phases are finally integrated and contribute to the variation of acquired signal. Under the assumption of uniform rigid motion during the sequence execution in a single shot, the motion operator $T_{vt}R_{\omega t}$ represented by velocities v_{RO}, v_{PE} and angular velocity ω is applied to s_0 of each spin to update the coordinate:

$$ \begin{bmatrix} x_t \\ y_t \end{bmatrix} = T_{vt}R_{\omega t} \begin{bmatrix} x_0 \\ y_0 \end{bmatrix} \tag{8} $$

where T_{vt} is translation operator and $R_{\omega t}$ is rotation operator at time t. The rigid motion parameters can be visualized as velocity fields at pixel level as:

$$ \begin{aligned} V_{RO}(x,y) &= -\omega \cdot y + v_{RO} \\ V_{PE}(x,y) &= \omega \cdot x + v_{PE} \end{aligned} \tag{9} $$

2) B_1^+ inhomogeneity: The B_1^+ (radio frequency field) inhomogeneity is taken as the sum of simple low-order polynomial functions with random number set r_p and Gaussian functions
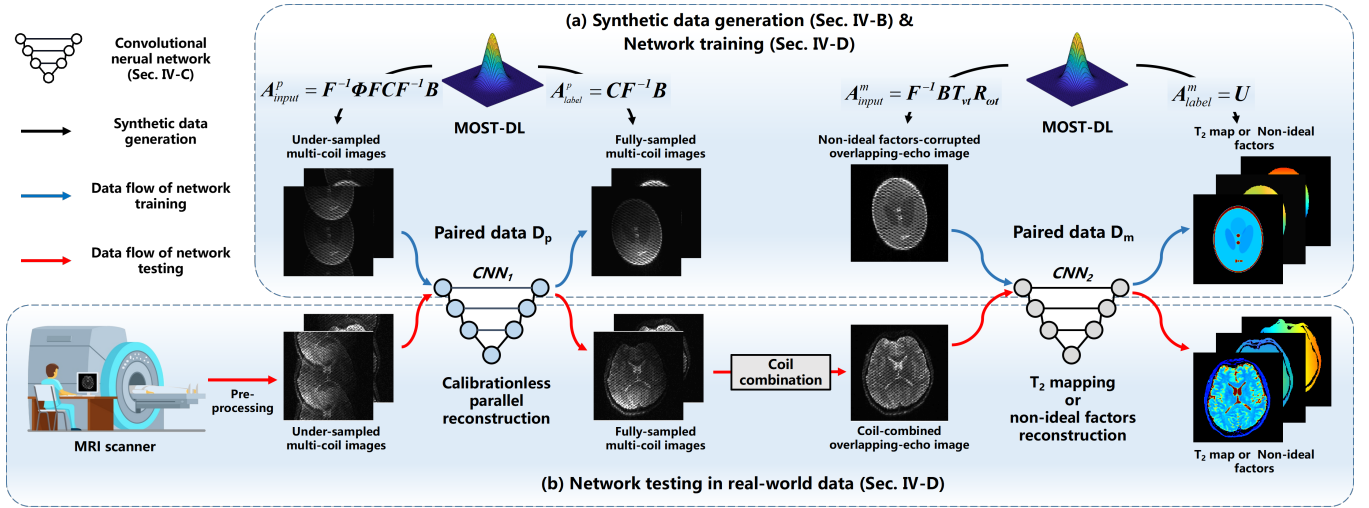
Fig. 2. Overview of the proposed pipeline for application in T_2 mapping under head motion. (a) Synthetic data generation and network training: paired dataset D_p and D_m were generated by the MOST-DL framework and used for CNN_1 and CNN_2 training; (b) Network testing in real-world data: raw data from MRI scanner can be parallel reconstructed and T_2 mapping by the trained CNN_1 and CNN_2. The non-ideal factors (e.g., velocity fields and B_1^+ field) can also be reconstructed for visualization. The multi-coil MR images are coil-combined to a single-coil image after CNN_1 reconstruction. F: Fourier operator; B: Bloch equation operator; U: down-sampling operation; $T_{vt}R_{\omega t}$: motion operator; Φ: sampling pattern for parallel imaging; C: coil sensitivity maps.

with random number set r_n:

$$\Delta B(x,y) = \sum_{n_x=1}^{N_p} \sum_{n_y=1}^{N_p} r_p(n_x, n_y) x^{n_x} y^{n_y} + \sum_{n_g=1}^{N_g} G(x,y; r_n(n_g)) \tag{10}$$

where, n_x and n_y are the order of x and y, respectively, n_g represents the superposition of Gaussian profiles. In this work, N_p is set to 2 and N_g is set to 1. Subsequently, ΔB will be normalized within a reasonable boundary to obtain the final B_1^+. The actual flip angle for each spin is calculated as a proportion of the desired flip angle.

3) Other non-ideal factors: The undesirable effects arising from eddy currents, system delays, nonlinear gradient amplifier response function, or even mechanical vibrations can cause gradient imperfections, which further results in the deviation of acquired k-space from its desired design. We model the gradient imperfections by simulating the random fluctuation of gradient area to cover the comprehensive effect caused by instrument imperfection. Besides, it is common practice to assume that the noise in MRI raw data have a Gaussian distribution with zero mean [40]. Due to the linear and orthogonal nature of Fourier transform, the real and imaginary images reconstructed from raw data will preserve the Gaussian characteristics of the noise. Therefore, noise of Gaussian distribution with same variance is added to the real/imaginary part of synthetic image. It is possible to expand the framework for other non-ideal factors (e.g., ΔB_0, B_1^-, chemical shift) and this is something that we are planning for future work.

D. Model-based Simulation and Signal Reconstruction

The model-based simulation in this framework is based on solving the Bloch equation with task-specific pulse sequence. By introducing the coil sensitivity map, the simulation can be extended from a single-coil scenario to a multi-coil scenario. The paired measurements b_s and b_t of different evolution

pathways derived from the same tissue relaxation parameters a_j can be obtained by controlling the non-ideal factors σ_k and adjusting the forward model A.

Under the MOST-DL framework, a faithful signal reconstruction relies on physical feasibility, adequate signal representation and the decoding ability of the learning model. To verify the accuracy of data modeling, the MOST-DL provides the possibility of reconstructing non-ideal factors by solving the optimization problem of Equation (5) only with the label changed to non-ideal factors. As such, the non-ideal factors carried in real-world data can be reconstructed explicitly (or visualized) and used as a quality control indicator for secondary validation of the reliability in data generation.

IV. MOLED T_2 MAPPING UNDER RIGID MOTION

The MOST-DL is applied to build synthetic datasets for MOLED T_2 mapping under rigid motion. In this application, the motion correction is jointly achieved by a cascade framework consists of two CNNs: CNN_1 for calibrationless parallel reconstruction to address the mismatch between under-sampled data and ACS data; CNN_2 for end-to-end mapping from motion-corrupted MOLED images to motion-free quantitative T_2 maps. Fig. 2 shows the data flow of synthetic data generation, network training and testing. The MOLED acquisition and reconstruction are reviewed in Section. IV-A. Paired datasets are generated by the MOST-DL according to the forward models as described in Section. IV-B. Section. IV-C describes the network architecture used for this application. Finally, the details of network training with synthetic data and testing with real-world data are provided in Section IV-D.

A. MOLED Acquisition and Reconstruction

Details of the topic have been presented previously [14], [15] but a brief summary is provided here. In overlapping-echo acquisition, multiple echo signals containing different
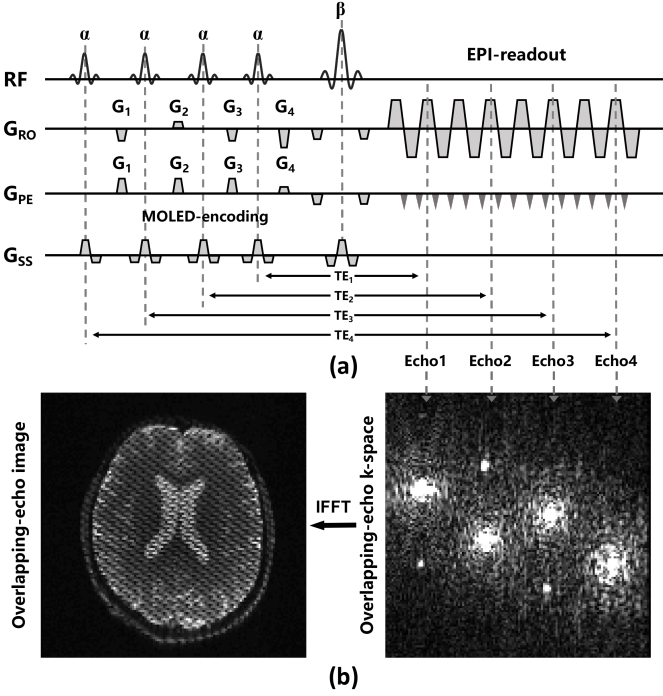
Fig. 3. (a) Single-shot SE-MOLED sequence for T_2 mapping. The four TEs of the SE-MOLED sequence are 22.0, 52.0. 82.0, 110.0 ms in this work, corresponding to the four excitation pulses. (b) The overlapping-echo image and k-space data.

information (e.g., relaxation [15], diffusion [16] and multi-slices [41]) are encoded in a single k-space to achieve efficient signal compression. These echo signals with different evolution times are prepared by independent RF pulses and are finally acquired with overlapped high-frequency components. The 2D SE-MOLED sequence [15] as shown in Fig. 3(a) can be used to acquire echo signals following the T_2 signal decay for T_2 mapping. Four excitation pulses with the same flip angle $\alpha = 30°$ are followed by a refocusing pulse with a flip angle of $\beta = 180°$ to generate four main T_2-weighted spin echoes with different TEs (TE$_1$ = 22.0 ms, TE$_2$ = 52.0 ms, TE$_3$ = 82.0 ms, TE$_4$ = 110.0 ms). The gradients G_1, G_2, G_3 and G_4 are echo-shifting gradients, which are used to shift the four echoes away from the k-space center along the phase-encoding and frequency-encoding directions. The four echo signals with different evolution times are obtained in the same k-space, resulting in an image modulated by interference fringes as shown in Fig. 3(b). The complexity of the acquired signal increases greatly due to the overlapped echoes. Therefore, a deep neural network was used to perform direct end-to-end mapping reconstruction without echo separation.

B. Synthetic Data Generation by MOST-DL

Only T_2 and M_0 templates were used in synthetic data generation, in which $T_2 \in [0, 650]$ ms, $M_0 \in [0, 1]$. The T_1 value was fixed to 2000 ms for all simulations and tissues due to the short duration between the four excitation pulses (about 44 ms). Random rotations (0°, 90°, 180°, 270°) and flips (horizontal and vertical) were applied to the parametric templates for data augmentation.

Fig. 2(a) shows the pipeline of synthetic data generation relied on MOST-DL framework. For parallel reconstruction task in CNN$_1$, the paired dataset D_p was generated following the forward models $\boldsymbol{A}_{input}^p$ and $\boldsymbol{A}_{label}^p$ as:

$$\begin{cases} \boldsymbol{A}_{input}^p = \boldsymbol{F}^{-1}\boldsymbol{\Phi}\boldsymbol{F}\boldsymbol{C}\boldsymbol{F}^{-1}\boldsymbol{B} \\ \boldsymbol{A}_{label}^p = \boldsymbol{C}\boldsymbol{F}^{-1}\boldsymbol{B} \end{cases} \tag{11}$$

in which, $\boldsymbol{F}$ is the Fourier operator, $\boldsymbol{B}$ is the Bloch operator for 2D SE-MOLED sequence, $\boldsymbol{\Phi}$ is the sampling pattern, $\boldsymbol{C}$ is the coil sensitivity maps. Due to the nature of EPI readout, a uniform under-sampling with central region not fully-sampled was used as $\boldsymbol{\Phi}$, and the acceleration rate R = 2. The multi-coil overlapping-echo images were generated from the multiplication of synthetic single-coil overlapping-echo images and coil sensitivity maps obtained from offline collected ACS data. These ACS data were collected by conventional GRAPPA scanning protocol and a sensitivity maps pool containing about 100 slices was generated using the ESPIRiT algorithm [42]. For the end-to-end T_2 mapping and non-ideal factors reconstruction task in CNN$_2$, the paired dataset D_m was generated follow the forward models $\boldsymbol{A}_{input}^m$ and $\boldsymbol{A}_{label}^m$ as:

$$\begin{cases} \boldsymbol{A}_{input}^m = \boldsymbol{F}^{-1}\boldsymbol{B}\boldsymbol{T}_{vt}\boldsymbol{R}_{\omega t} \\ \boldsymbol{A}_{label}^m = \boldsymbol{U} \end{cases} \tag{12}$$

where $\boldsymbol{U}$ is the down-sampling operation (applied on spin-level parametric templates for T_2 mapping and non-ideal factors for velocity fields and B_1^+ reconstruction). As mentioned above, the rigid motion as a main non-ideal factor can be described by the motion operator $\boldsymbol{T}_{vt}\boldsymbol{R}_{\omega t}$. The corresponding T_2 templates, velocity fields and B_1^+ with size of 512×512 were down-sampled to 256×256 as labels. During Bloch simulation, all RF pulses were simulated using hard pulses with spatial B_1^+ inhomogeneity. Gradient fluctuation was applied in MOLED echo-shifting gradients. The step size in time was 0.003 ms for readout gradients and 0.1 ms for other gradients. GRAPPA was not considered in synthetic data, and the echo spacing (ESP) of readout gradients was 1/R of that in the *in vivo* experiment in order to maintain a consistent echo train length (ETL). The detailed imaging parameters were ESP = 0.465 ms, field of view (FOV) = 22 × 22 cm^2, and matrix size = 128 × 128. Gaussian noise was added in single-/multi-coil overlapping-echo images.

For domain randomization, we randomized the following aspects of the synthetic domain:

- Distribution of T_2 value of parametric templates;
- SNR of multi-coil/single-coil MR images: 30.0 to ∞ dB;
- Gradient fluctuation for MOLED echo-shifting gradients: -5% to 5%;
- B_1^+ inhomogeneity of excitation pulses: 0.7 to 1.2;
- The velocities v_{RO} and v_{PE}: -10.0 to 10.0 cm/s, and the angular velocity, ω: -50.0 to 50.0 °/s;
- Randomly matching of coil sensitivity maps and synthetic single-coil images for generating multi-coil images;

Other factors were considered to have no significant contribution to these two tasks and were therefore ignored.

Finally, 8,000 paired samples (under-sampled multi-coil images vs. fully-sampled multi-coil images) were generated for
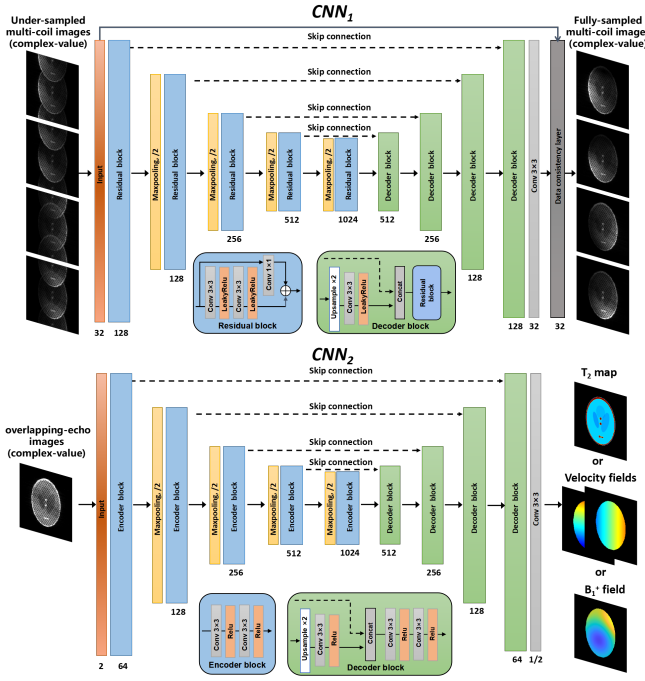
Fig. 4. The proposed CNN$_1$ and CNN$_2$ architectures. The network backbone is based on U-Net, which consists of series of encoder blocks and decoder blocks.

CNN$_1$ training, and 15,000 paired samples (overlapping-echo images vs. T$_2$ maps/velocity fields/B$_1^+$ fields) were employed for CNN$_2$ training. The Bloch simulation was implemented in MRiLab [43] and SPROM software [44] on a machine with an NVIDIA GeForce RTX 2080 Ti GPU. Other processes were performed using MATLAB (R2019b) software (Mathworks, Natick, MA, USA).

C. Network Architecture

Our network backbone is based on five-level U-Net [45], which consists of series of encoder blocks to extract high-dimensional features from original MR images and decoder blocks to reconstruct target signals. The detailed CNN$_1$ and CNN$_2$ architectures are shown in Fig. 4. In CNN$_1$, a residual learning block is used as encoder block and a data consistency layer [46] is introduced for parallel reconstruction. The value of empirical parameter λ of the data consistency layer is set to 1.0 for denoising, which represents the reconstructed result is the combination of the CNN prediction and the original measurement. In both CNN$_1$ and CNN$_2$, up-sampling operation in decoder block were carried out through bilinear interpolation instead of up-convolution. The final output was generated using the last 3×3 convolution layer without activation function. The amount of trainable parameters for CNN$_1$ and CNN$_2$ were 52.7 M and 34.5 M, respectively.

D. Training and Testing Details

Fig. 2(a) illustrates the data flow of network training. Parallel reconstruction and end-to-end T$_2$ mapping tasks both affect the final result but are independent of each other, so we trained CNN$_1$ and CNN$_2$ separately using datasets D_p and D_m, respectively. For CNN$_2$, the non-ideal factors reconstruction

only serve as visual quality control and do not affect T$_2$ mapping. Therefore, the same network structure was used but with different network parameters to map from overlapping-echo images to different modalities (T$_2$ map, velocity fields or B$_1^+$ field). Besides, before fed into CNN$_2$, the overlapping-echo image (128×128) was first zero-padded in k-space to 256×256 and then normalized by the maximum value of magnitude in image domain. The paired samples were randomly cropped into 96×96 patches during the CNN$_2$ training phase because the MOLED echo signals with different evolution times were encoded in the local modulation. However, the patching operation is not necessary in the testing phase due to the sliding window manner of convolution.

For both CNN$_1$ and CNN$_2$, the paired synthetic data sets were randomly split into 90% and 10% for training and validation. The complex-valued multi-/single-coil overlapping-echo images were divided into real and imaginary components as two individual channels for the network input [46]. We used l_1 norm as the loss function and Adam optimizer with momentum parameters $\beta_1 = 0.9$ and $\beta_2 = 0.999$ to update network parameters. The initial learning rate was 10^{-4}, which decreased by 20% after each 80,000 iteration until the network converged. Finally, the best models of CNN$_1$ and CNN$_2$ with the lowest loss on the validation set were selected for testing purpose.

The data flow of network testing is shown in Fig. 2(b). The raw data acquired from MRI scanner was first pre-processed, including intensity scaling and 3-line linear phase correction to remove EPI Nyquist ghosting. The multi-coil data reconstructed from network CNN$_1$ were coil-combined by an adaptive coil combination algorithm [47], in which the coil with the highest SNR was selected as the reference coil. Before fed into CNN$_2$, the coil-combined 128×128 overlapping-echo image was also zero-padded to 256×256 in k-space and then normalized in image domain. The network training and testing were implemented in Python using the PyTorch library on a machine with an NVIDIA GeForce RTX 2080 Ti GPU. The pre-processing and coil combination for real-world data were performed using MATLAB (R2019a) software (Mathworks, Natick, MA, USA).

E. Validation Experiments

The study protocol was approved by the institutional research ethics committees, and written informed consents were obtained from the volunteers and the patient's guardians prior to the experiments.

1) Numerical Human Brain Experiments: We first conducted numerical human brain experiments with known quantitative parameters. The original parametric templates were also generated from a multi-contrast volume selected from the IXI database following the MOST-DL pipeline. The parametric templates, including T$_2$ $\in$[0, 600] ms and M$_0$ $\in$[0, 1], were used as the ground-truth to evaluate the reconstruction performance. The forward operators in Equations (11) and (12) were applied to obtain single/multi-coil overlapping images for network testing. The imaging parameters were consistent with that for training data, and Gaussian noise was added in numerical brain to achieve SNR of 34.0 dB.
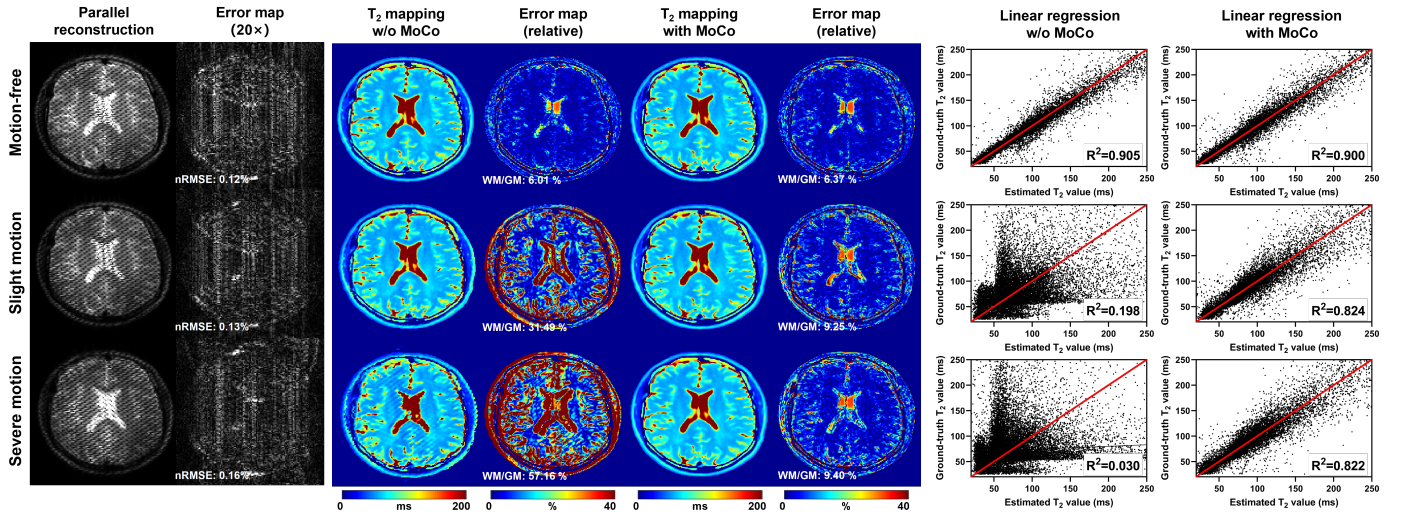
Fig. 5. Parallel reconstruction and T_2 mapping results in numerical brain using MOST-DL method from data with motion-free (row 1), slight motion (row 2) and severe motion (row 3). The T_2 range of linear regression analysis is 20 to 250 ms. Slight motion: v_{RO} = -2.0 cm/s, v_{PE} = -2.0 cm/s, ω = -10.0 °/s; Severe motion: v_{RO} = -8.0 cm/s, v_{PE} = -5.0 cm/s, ω = -32.0 °/s. MoCo: Motion correction.

2) In Vivo Experiments: The *in vivo* experiments in this section were conducted on a whole-body MRI system at 3T (MAGNETOM Prisma TIM, Siemens Healthcare, Erlangen, Germany) with a 16-channel head coil. All motion-related *in vivo* data were acquired from four healthy volunteers and a patient with epilepsy using SE-MOLED sequence. The healthy volunteers were instructed for three scans: (1) reference scan, (2) motion-free scan and (3) continuous motion scan. The reference scan was employed only once at the beginning of the whole scan time to obtain ACS data. The (2) and (3) scans used parallel imaging and the acceleration factor R = 2. In the motion-corrupted scan, the subjects were asked to randomly move their head. This scan was repeated several times with each session lasting 80 s. Besides, a healthy volunteer was instructed for an additional scan with continuous nodding to explore the performance of the proposed method under through-plane motion. The patient data were obtained by appending the SE-MOLED sequence in a standard clinical exam. The relevant imaging parameters include FOV = 22×22 cm^2, matrix size = 128×128, slice thickness = 4 mm, slice number = 21, ESP = 0.93 ms. For comparison, a conventional spin-echo (SE) sequence was acquired on the four healthy volunteers with parameters: TEs = 35, 50, 70, 90 ms. We also collected additional motion-free SE-MOLED data from another 15 healthy volunteers for network training in comparison methods. Among these, the ACS data from 5 healthy volunteers were used to form a sensitivity maps pool for multi-coil images simulation.

3) Comparative Algorithms: We used two calibration-based parallel reconstruction methods (GRAPPA [18] and ESPIRiT [42]) and three calibrationless methods (SAKE [20], ALOHA [21], real data-driven deep learning [23]) to verify the performance of our parallel reconstruction method in *in vivo* experiments. Due to the difficulty in obtaining the fully-sampled ground-truths of the SE-MOLED sequence, we used the GRAPPA reconstructed results as labels for the real data-driven deep learning method, and the CNN_1 was trained for a fair comparison. For motion correction, we conducted compar-

ative experiments using different motion simulation strategies. Image-domain simulation strategy (similar to Johnson *et al.* [26]) and k-space simulation strategy (similar to Duffy *et al.* [27]) were used as comparative methods. The CNN_2 was selected as the motion correction network for all simulation strategies. The simulation parameters of velocities v_{RO}, v_{PE} and angular velocity ω were consistent with that for MOST-DL. Additionally, self-comparison experiments of domain randomization were conducted to evaluate the impact of noise, B_1^+ inhomogeneity, gradient fluctuation, T_2 distribution and motion correction.

V. RESULTS

A. Experiments with Numerical Human Brain

In Fig. 5, the results of parallel reconstruction (CNN_1) and T_2 mapping (CNN_2) under different levels of rigid motion are plotted. In all cases, the parallel reconstruction results show high quality with normalized root mean square error (nRMSE) values below 0.2%. For the motion-free case, the final T_2 maps reconstructed with/without motion correction are observed to be similar in both the quantitative maps and the error maps. With the inclusion of motion, the T_2 maps without motion correction become corrupted, causing a higher error compared with the ground-truth. In contrast, the motion-corrected maps remain high quality with low error levels ($<10\%$ relative error) in gray/white matter (GM/WM). These results are supported by linear regression analysis. The R^2 values show significant improvement after motion correction (from 0.198 to 0.824 in slight motion case, from 0.030 to 0.822 in severe motion case).

B. Experiments with Real Data

Fig. 6 shows the parallel reconstruction results of *in vivo* human brain using various comparison methods and the proposed MOST-DL-based method (with CNN_1). To compare the results quantitatively, we also calculate the ghost-to-signal ratio (GSR) value. For the motion-free case, both calibration-based and calibrationless methods performed well and have
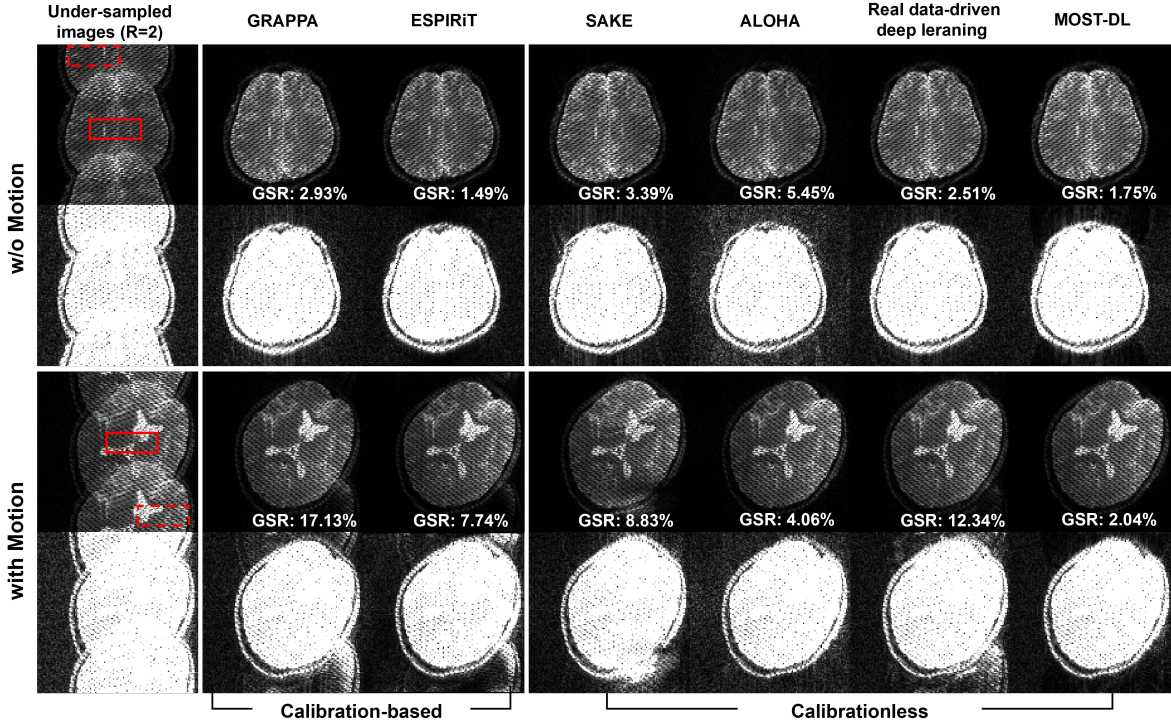
Fig. 6. Parallel reconstruction results of under-sampled SE-MOLED images by various methods. The ten times re-scaled images are shown below the original images. The GSR values were calculated using the mean magnitude in regions marked by red solid boxes (signal) and red dotted boxes (ghost).

low GSR values. However, in the motion-corrupted cases, significant artifacts appear in calibration-based results due to the mismatch between reference scan and motion-corrupted scan. SAKE and real data-driven deep learning methods also face challenges in motion-corrupted cases that visible artifacts are presented in scaled images. Both the proposed method and ALOHA eliminated all visible artifacts, however, compared with MOST-DL, ALOHA has a higher GSR value and reconstruction fails in some cases.

Fig. 7(a) illustrates the results of T_2 mapping (with CNN_2) from 3 healthy volunteers. One can see that the motion-corrupted cases (parallel reconstruction by GRAPPA) suffered from ghosting artifacts (marked by red arrows) and motion artifacts (marked by yellow arrows). With the application of the proposed MOST-DL to parallel reconstruction and motion correction, these artifacts are eliminated, and the image quality is significantly improved compared with motion-corrupted cases. Quantitative analysis of T_2 values between motion-corrupted/motion-corrected cases and motion-free cases are shown in Fig. 7(b-c). The T_2 values were calculated from 36 regions of interest (ROIs,12 ROIs of each subject) placed within the regions mostly affected by motion artifacts(gollobus palludis, frontal white matter and insular cortex) after registra-tion. The regression plots in Fig. 7(a) show better consistency between motion-corrected cases and motion-free cases (R^2 = 0.944) compared with motion-corrupted cases (R^2 = 0.432). These results are supported by the Bland-Altman plots (Fig. 7(c)) that the motion-corrupted cases show a broader range of differences: motion-corrupted cases: mean difference = 2.54 ms, upper and lower limits of agreement = -12.9 ms and 18.0

ms; motion-corrected cases: mean difference = 0.98 ms, upper and lower limits of agreement = -3.58 ms and 5.44 ms.

C. Effects of Motion Simulation Strategy

To verify our claim that high-precision motion simulation plays a key role in motion correction and T_2 mapping, we compared our proposed method with various motion simu-lation strategies. Note that the multi-coil MOLED images have been parallel reconstructed by trained CNN_1. As shown in Fig. 8(a), signal corruption (marked by yellow arrows, image-domain transformation) and signal loss (marked by green arrows, k-space transformation) appear in retrospective motion simulation methods. In contrast, the proposed MOST-DL (prospective method) gives closer result to the real-world data. In Fig. 8(b), we can see that there are still residual motion artifacts by using the retrospective motion simulation method, and the reconstruction even fails in some cases. We believe that the inaccurate motion simulation is the main source of error in final T_2 mapping results.

D. Effects of Domain Randomization

Here, we verify that the domain randomization during the data generation stage has a significant effect on the final MOLED T_2 mapping results. The reference T_2 maps were obtained using SE sequence. The quantitative analysis (linear regression) is presented in TABLE 1 from manually segmented ROIs (thalamus, caudate nucleus, putamen, gollobus palludis, frontal white matter and insular cortex) of 3 healthy volunteers in motion-free results. The full domain randomization exhibits
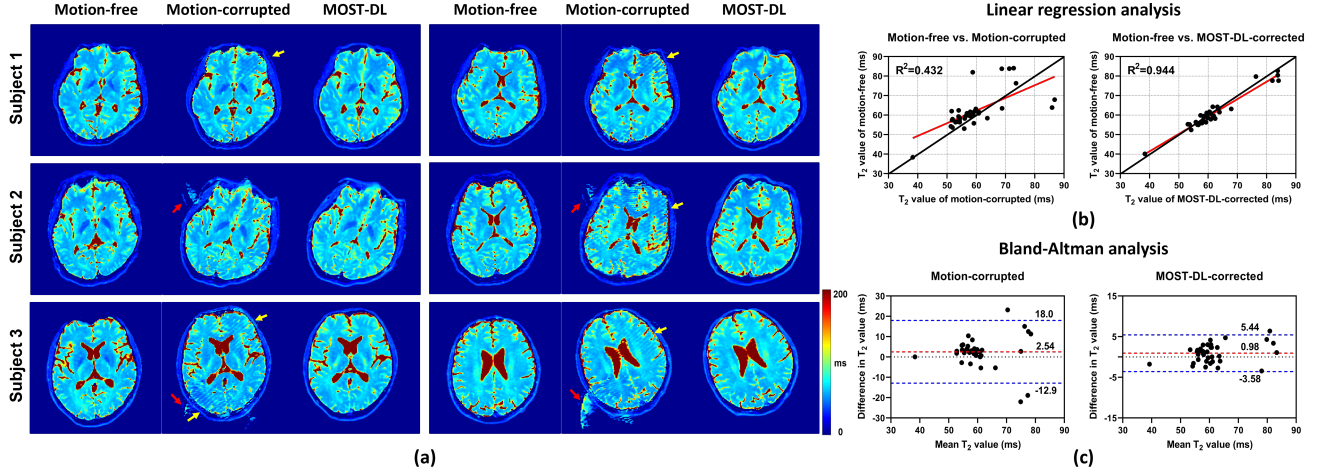
Fig. 7. The final T_2 mapping results from *in vivo* data. (a) T_2 mapping results of different slices with in-plane motion from 3 subjects. The ghosting artifacts are marked by red arrows and the motion artifacts are marked by yellow arrows. (b) Linear regression plots for the comparison of motion-corrupted and MOST-DL-corrected with motion-free reference. (c) The Bland-Altman plots corresponding to the linear regression plots shown in (b). In the Bland-Altman plots, the blue dotted lines represent 95% confidence level, and the red dotted lines represent mean T_2 value differences.
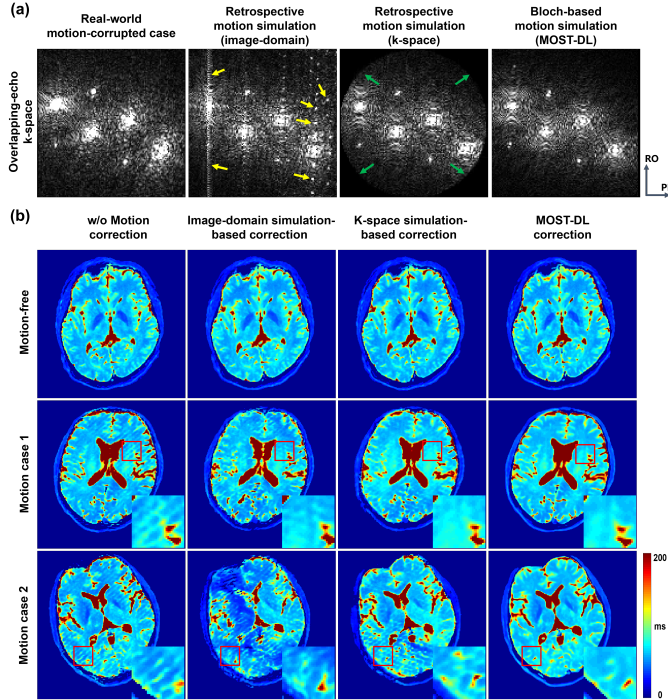

Fig. 8. Motion correction results using various motion simulation methods. (a) Overlapping-echo k-space from real-world motion-corrupted case and various motion simulation methods. The signal loss (marked by green arrows) and signal corruption (marked by yellow arrows) appear in retrospective motion simulation methods. (b) The results of T_2 mapping without motion correction, with retrospective motion simulation correction and MOST-DL correction in motion-free (upper row) and two motion cases (middle and lower rows).

the highest R^2 value of linear regression. As for motion-corrupted cases in Fig. 9(a), considerable motion artifacts remain in the T_2 maps produced by MOST-DL without motion randonmization. These motion artifacts are obliquely striped and primarily distributed in the region of frontal white matter and insular cortex. The mean and variance T_2 value curves in Fig. 9(b) show that the stability of the results without

motion randomization is significantly lower and accompanied by greater variance, which means that motion artifacts heavily influence the T_2 values within the ROIs. Furthermore, it can be noticed that the negative effect of motion artifacts becomes greater as the T_2 value rises.

TABLE I
SELF-COMPARISON OF DOMAIN RANDOMIZATION (DR)

Evaluation type	R^2 of linear regression		
	Subject 1	Subject 2	Subject 3
Full DR	**0.981**	**0.930**	**0.988**
w/o B_1^+ inhomogeneity	0.976	0.918	0.952
w/o Noise added	0.980	0.923	0.988
w/o Gradient fluctuation	0.980	0.901	0.970
w/o Random T_2 distribution	0.969	0.911	0.975

E. Reconstruction of Non-ideal Factors

As secondary validation of the reliability of our method in data generation, the non-ideal factors, velocity fields and B_1^+ field, were reconstructed by retrained network CNN_2. To obtain references for velocity fields, more of the same echo trains and the refocusing pulses were intentionally appended to the original SE-MOLED sequence, which result in four MR images to record the subject motion. Subsequently, four MR images are used to calculate three sets of parameters of rigid motion (i.e., translation (mm) along the x and y directions and rotation (degree) in the plane) using Statistical Parametric Mapping (SPM) software. Then, v_{RO}, v_{PE}, and ω are obtained by regressing the motion parameters and the time between excitation pulses and refocusing pulses. The reference velocity fields are generated according to Equation (9). For B_1^+ fields, the references were obtained using the Siemens product B_1^+ map based on turbo-flash sequence. Fig. 10 illustrates the reconstructed velocity fields, B_1^+ field and the corresponding reference from same slice during different motion states. We can see that both the predicted results agree well with their references.
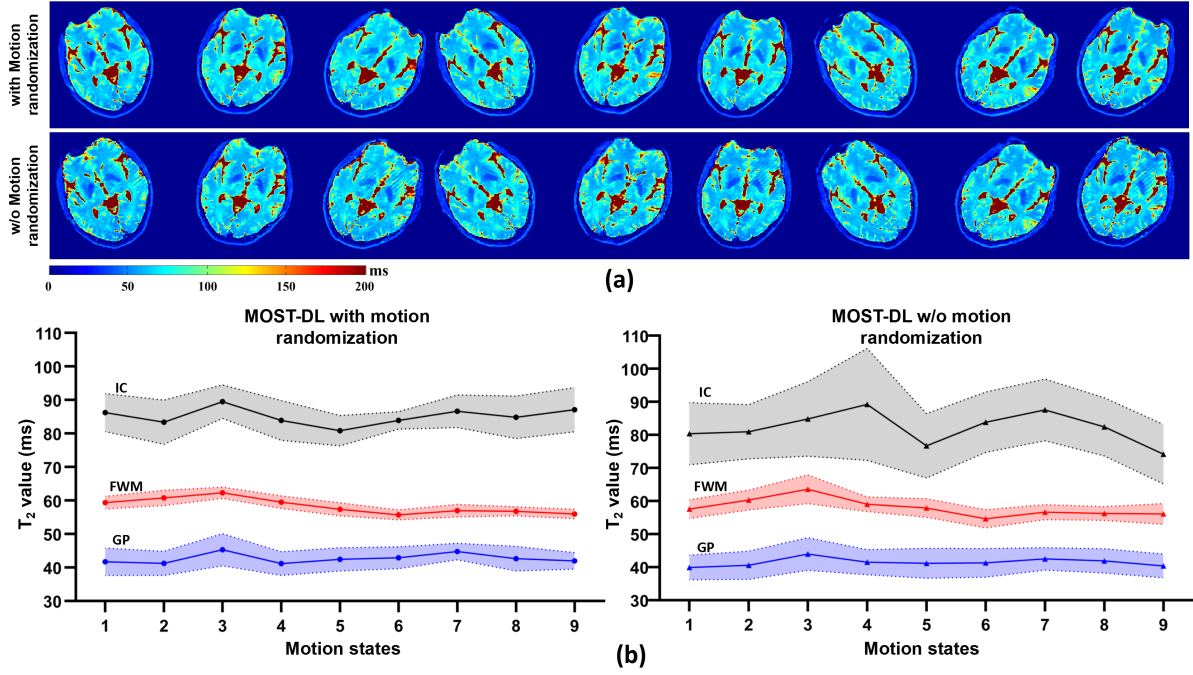
Fig. 9.   Self-comparison of domain randomization in rigid motion. (a) Sequential T_2 maps produced by MOST-DL with and without motion randomization from representative slice. (b) Mean and variance T_2 value curves from 3 ROIs of 9 motion states in (a). IC: Insular cortex; FWM: Frontal white matter; GP: Globus pallidus.
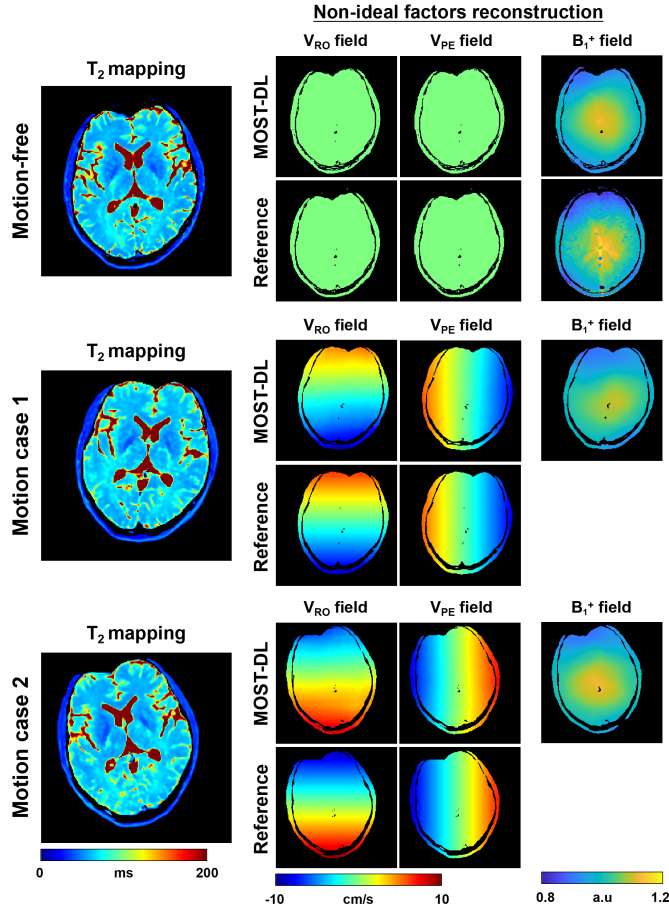

Fig. 10.   Non-ideal factors reconstruction results (velocity fields and B_1^+ fields left to right) of a representative slice during different motion states in motion-free (upper row) and two motion cases (middle and lower rows).

F. Effects of Through-plane Motion

Although through-plane motion correction is challenging for 2D pulse sequences, we also explored the effect of it on the current method. To capture the through-plane motion synchronously with T_2 mapping, the SE-MOLED sequence with four echo trains was also used as mentioned above. The through-plane velocity was estimated based on the duration of each echo train and the change in signal strength relative to the motion-free case. When the signal is abnormally attenuated (or disappeared), we assume that through-plane motion beyond the slice thickness has occurred during the time interval between the excitation pulse and refocusing pulse. The excitation slice thickness is 4.0 mm, while the refocusing slice thickness is 3.0 mm. All assessments were performed under the assumption that the subject was nodding at a uniform velocity due to the narrow sampling window within 300 ms. Fig. 11 illustrates the results of T_2 mapping under such through-plane motion. The T_2 maps were reconstructed with good image quality under slight (<1.5 cm/s) and medium (1.5 cm/s$\sim$3.5 cm/s) through-plane motion. Severe through-plane motion (>3.5 cm/s) strongly impacts original MRI signals and degrades the final T_2 map.

G. An Example of A Clinical Case

Fig. 12 shows the results of a 10-year-old patient with epilepsy. Strong streak artifacts from motion are observed in the anatomical images (T_1 MPRAGE sequence, Fig. 12(a)) and T2WI (TSE sequence, Fig. 12(b)), which present challenges on quantitative measurement of hippocampal T_2. The results reconstructed with the proposed method from the MOLED data are shown in Fig. 12(c). We can see that the proposed method achieves T_2 maps with high quality without motion
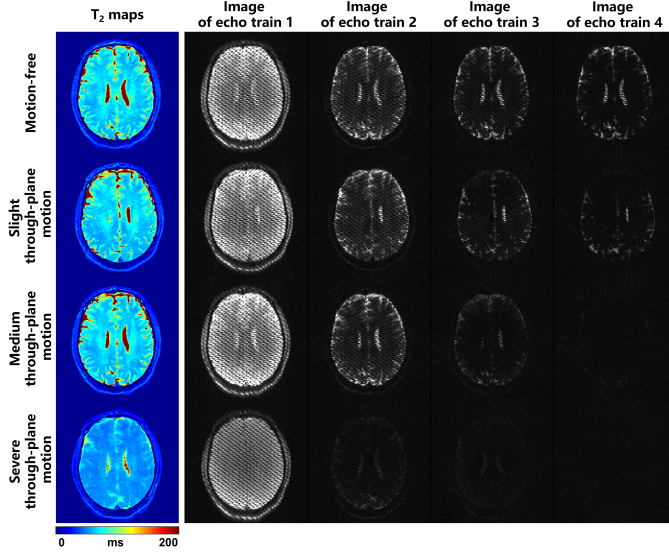
Fig. 11. T_2 mapping and the corresponding overlapping-echo images of four echo trains under through-plane motion. From top to bottom: cases of Motion-free, Slight motion: <1.5 cm/s; Medium motion: 1.5 cm/s~3.5 cm/s; Severe motion: >3.5 cm/s.
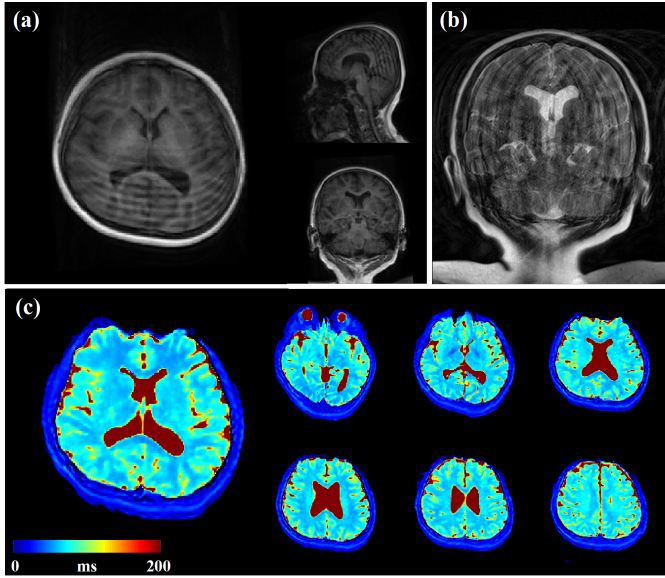

Fig. 12. The results from a 10-year-old patient with epilepsy. (a) MR images from T_1 MPRAGE sequence. (b) MR image from T_2 TSE sequence. (c) The T_2 maps reconstructed by the proposed method.

artifacts. Since the patient motion occurred randomly, it is difficult to evaluate if there is severe motion during the MOLED scan. However, we observe that the single-shot acquisition is more robust to unpredictable motion compared with multi-shot acquisition.

VI. DISCUSSION

A. Learning from Synthetic Data

In this work, we developed a synthetic data generation framework using public multi-contrast database to solve challenging quantitative MRI problems under severe head motion. The neural network is trained with synthetic dataset and can be well generalized to *in vivo* experimental data without

network fine-tuning. Two factors are considered to play crucial roles, i.e., (1) generating data using rich anatomical texture priors from public database, (2) the accurate modeling of the forward operator and non-ideal factors (especially subject motion in the Bloch simulation) with domain randomization. The tissue relaxation parameters in previous studies were created by randomly filling blank templates with hundreds of different basic geometric shapes such as circle, triangle and rectangle, which can render the texture of the reconstruction results match the real situation poorly. Moreover, accurate modeling makes the data distribution in the synthetic domain closer to that in the real domain. With domain randomization, discrepancies between the synthetic and real domains are modeled as variability, further making the data distribution of synthetic domain sufficiently wide. Unlike learning from real data, synthetic data does not depend on acquisition methods and experimental instruments but is only relevant to the signal model. This allows the network to focus on policy (model inversion) learning.

Recently, several deep-learning-based methods have been proposed to focus on reconstruction and motion correction for ultra-fast imaging sequences (e.g., single-shot EPI [23] or multi-shot EPI [48]). Due to the difficulty in obtaining paired fully-sampled or motion-free ground-truth, the reconstructed or motion-corrected results using traditional algorithms are usually used as labels for network training. In this work, the proposed MOST-DL-based method makes it possible to produce perfect data pairs from the first principle according to the forward physical model, with the flexibility to increase the diversity of the training data. As shown in Fig. 6, we compared the parallel reconstructed results of the human brain using real data (reconstructed labels) and synthetic data. The network trained from real data shows excellent performance in motion-free cases but degradation in the cases with motion. We believe that the reconstruction errors are likely caused by imperfect training data pairs and limited data patterns.

In MRI simulation, most deep learning-based motion-related methods simulate motion in acquired images using retrospective transformation, hence, the accuracy is always limited by pixel size and cannot fulfill the demand in this work. For intra-shot motion, the degree of motion is often far less than the size of a pixel between different phase lines. Therefore, we adopted a different method for motion simulation, which applied the motion operator in scanner coordinate system during Bloch simulation. The results in Fig. 8 show that retrospective motion simulation methods can lead to signal corruption and signal loss, which further degrade the final motion-corrected T_2 maps. Though the Bloch-based simulation might not accurately reflect all possible forms of real artifacts, the results show that the artifacts are most successfully eliminated.

Some novel unsupervised algorithms based on unpaired datasets have been published to overcome the lack of paired data in real world. Liu *et al.* [49] proposed a GAN-based framework to remove motion artifacts. They formulate the artifact removal problem as domain translation under the assumption that MR image is a nonlinear combination of content and artifact components. Though the paired data are not required, it is still necessary to manually distinguish

between artifact-free and artifact-corrupt images to build a large realistic training dataset. Oh *et al.* [50] convert motion artifact correction problem to subsampling MR reconstruction problem using the bootstrap subsampling and aggregation. However, as reported by the authors, this method faces challenges in intra-shot motion correction because the effect of intra-shot motion cannot be considered as sparse outliers in k-space.

We believe that synthetic data-based approach offers a new "unsupervised learning" paradigm and can take full advantage of supervised learning. Moreover, synthetic paired data can be more flexibly combined with existing deep learning methods to address challenging topics in medical imaging.

B. Non-ideal Factors Modeling and Reconstruction

The modeling and reconstruction of non-ideal factors is a key feature with great potential in the MOST-DL framework. Combined with more complex encoding in the signal acquisition process (e.g. MOLED encoding), MOST-DL can achieve sophistication that were previously impossible. As shown in Fig. 10, we first present results of 2D rigid motion estimation at pixel level (velocity fields) of single-shot acquisition without any motion-navigator. Motion information is often obtained from time series using image registration-based algorithms or tracking devices. For example, some approaches rely on motion-resolved imaging, which is achieved by modeling the signal correlation between different motion states along an additional motion-dedicated dimension [12]. However, these methods require acquisition of a large number of time frames for a specific task. In contrast, with the help of MOST-DL framework, we consider the motion estimation problem as a problem of non-ideal factor reconstruction, since the subject motion will bring extra phase accumulation and result in phase mismatch and artifacts. With paired synthetic data, the network is trained to learn motion pattern from motion-corrupted images with various levels of rigid motion and the results are mostly confirmed in *in vivo* experiments. The reason may be that motion alters data distribution so that it can be distinguished by the neural network, as reported by Liu *et al.* [49]. Similarly, under the MOLED encoding and MOST-DL decoding, the B_1^+ field inhomogeneity can also be reconstructed, which provides a new way for B_1^+ mapping at high efficiency.

In addition, non-ideal factor modeling and reconstruction opens a door to explore the domain gap between synthetic and real data. Specifically, during data generation, the MOST-DL framework allows modeling of arbitrary new non-ideal factors to explore whether they affect the final results. Then, the non-ideal factors reconstruction provides a visual representation of the added non-ideal factors to validate the modeling plausibility. For example, in this work, subject motion was modeled as a major non-ideal factor to generate training data for motion correction in T_2 mapping. The velocity fields estimation does not serve motion correction but provides a visualization of the instantaneous motion state, i.e., it explicitly indicates the motion information carried in the original data. By comparing with the reference velocity field, we have reason to believe

that the motion modeling in the data generation is consistent with the real situation.

C. Extensions and Limitations

The proposed method is not limited to the MOLED sequence and can be extended to other MRI pulse sequences, and even other fields of model-based medical imaging. Expansion requires a full understanding of the physical model and consideration of the impact of various non-ideal factors. In principle, the generalizability of MOST-DL relies heavily on the versatility of the Bloch simulation in MRI signal evolution. For example, in inter-shot motion correction, a multi-shot pulse sequence (e.g., multi-shot EPI or TSE sequence) is needed for simulation with different motion patterns between shot to shot. The proposed Bloch-based motion modeling is still suitable for multi-shot acquisition and facilitates the correction of small subject motions at the sub-voxel level. Because it is beyond the scope of this article, the relevant results are not provided.

There are still several limitations in the proposed method. First, the public multi-contrast MRI datasets used for parametric templates generation is not always sufficient in some specific anatomical regions such as abdomen, prostate and knee. However, an increasing number of techniques have been proposed for missing MRI contrast synthesis. For example, Sharma *et al.* [51] and Yurt *et al.* [52] present frameworks to generate one or more missing contrasts by leveraging redundant information using GAN. These techniques could be applied to our proposed framework for relaxation parameters generation. Second, our method only simulates the in-plane rigid motion under the 2D MOLED acquisition, and severe through-plane motion still degrade the final results. Future work will focus on adapting the framework to 3D or non-rigid motion, which is increasingly used in clinical practice. Finally, the Bloch simulation used for data generation suffers from high computational costs even with GPU acceleration. More efficient data generation technique is expected and will benefit our proposed supervised learning framework and reinforcement learning in medical imaging.

VII. CONCLUSION

In this article, a general scheme for synthetic data generation called MOST-DL was introduced. It was applied to solve a challenging problem of quantitative MRI under subject motion and non-ideal RF field. The results suggest that the MOST-DL method can generate synthetic images comparable to real data in quality, and achieve high performance in parallel reconstruction and motion correction. We believe that the proposed framework could be applied to similar problems with other MRI acquisition methods and in other modalities of medical imaging.

REFERENCES

[1] Y. LeCun, Y. Bengio, and G. Hinton, "Deep learning," *Nature*, vol. 521, no. 7553, pp. 436-444, May. 2015.

[2] G. Litjens, T. Kooi, B. E. Bejnordi *et al.*, "A survey on deep learning in medical image analysis," *Med. Image Anal.*, vol. 42, pp. 60-88, Dec. 2017.

[3] J. Tremblay, A. Prakash, D. Acuna *et al.*, "Training deep networks with synthetic data: Bridging the reality gap by domain randomization," *in Proceedings of IEEE Conference on Computer Vision and Pattern Recognition*, 2018, pp. 1082-1090.

[4] A. F. Frangi, S. A. Tsaftaris and J. L. Prince, "Simulation and synthesis in medical imaging," *IEEE Trans. Med. Imag.*, vol. 37, no. 3, pp. 673-679, Mar. 2018.

[5] A. Gilbert, M. Marciniak, C. Rodero, P. Lamata, E. Samset, and K. McLeod, "Generating synthetic labeled data from existing anatomical models: An example with echocardiography segmentation," *IEEE Trans. Med. Imag.*, vol. 40, no. 10, pp. 2783-2794, Oct. 2021.

[6] A. Gilbert, M. Marciniak, C. Rodero, P. Lamata, E. Samset, and K. McLeod, "A framework for the generation of realistic synthetic cardiac ultrasound and magnetic resonance imaging sequences from the same virtual patients," *IEEE Trans. Med. Imag.*, vol. 37, no. 3, pp. 741-754, Feb. 2018.

[7] N. Duchateau, M. Sermesant, H. Delingette and N. Ayache, "Model-Based generation of large databases of cardiac images: Synthesis of pathological cine MR sequences from real healthy cases," *IEEE Trans. Med. Imag.*, vol. 37, no. 3, pp. 755-766, Mar. 2018.

[8] F. Mahmood, D. Borders, R. J. Chen *et al.*, "Deep adversarial training for multi-organ nuclei segmentation in histopathology images," *IEEE Trans. Med. Imag.*, vol. 39, no. 11, pp. 3257-3267, 2020.

[9] R. J. Chen, M. Y. Lu, T. Y. Chen, D. F. K. Williamson, and F. Mahmood, "Synthetic data in machine learning for medicine and healthcare," *Nat. Biomed. Eng.*, vol. 5, no. 6, pp. 493-497, Jun. 2021.

[10] F. Mahmood, R. Chen and N. J. Durr, "Unsupervised reverse domain adaptation for synthetic medical images via adversarial training," *IEEE Trans. Med. Imag.*, vol. 37, no. 12, pp. 2572-2581, Dec. 2018.

[11] G. Cruz, O. Jaubert, T. Schneider *et al.*, "Rigid motion-corrected magnetic resonance fingerprinting," *Magn. Reson. Med.*, vol. 81, no. 2, pp. 947-961, Feb. 2019.

[12] S. Ma, N. Wang, Y. Xie *et al.*, "Motion-robust quantitative multiparametric brain MRI with motion-resolved MR multitasking," *Magn. Reson. Med.*, vol. 87, no. 1, pp. 102-119, Aug. 2021.

[13] M. J. Fair, F. Wang, Z. Dong *et al.*, "Propeller echo-planar time-resolved imaging with dynamic encoding," *Magn. Reson. Med.*, vol. 83, no. 6, pp. 2124-2137, Nov. 2019.

[14] C. B. Cai, Y. Q. Zeng, Y. C. Zhuang *et al.*, "Single-shot T2 mapping through overlapping-echo detachment (OLED) planar imaging," *IEEE Trans. Biomed. Eng.*, vol. 64, no. 10, pp. 2450-2461, Oct. 2017.

[15] J. Zhang, J. Wu, S. J. Chen *et al.*, "Robust single-shot T2 mapping via multiple overlapping-echo acquisition and deep neural network," *IEEE Trans. Med. Imag.*, vol. 38, no. 8, pp. 1801-1811, Aug. 2019.

[16] L. C. Ma, C. B. Cai, H. Y. Yang, *et al.*, "Motion-tolerant diffusion mapping based on single-shot overlapping-echo detachment (OLED) planar imaging," *Magn. Reson. Med.*, vol. 80, no. 1, pp. 200-210, Jul. 2018.

[17] C. B. Cai, C. Wang, Y. Q. Zeng *et al.*, "Single-shot T2 mapping using overlapping-echo detachment planar imaging and a deep convolutional neural network," *Magn. Reson. Med.*, vol. 80, no. 5, pp. 2202-2214, Nov. 2018.

[18] M. A. Griswold, P. M. Jakob, R. M. Heidemann *et al.*, "Generalized autocalibrating partially parallel acquisitions (GRAPPA)," *Magn. Reson. Med.*, vol. 47, no. 6, pp. 1202-1210, Jun. 2002.

[19] C. A. Baron, and C. Beaulieu, "Motion robust GRAPPA for echo-planar imaging," *Magn. Reson. Med.*, vol. 75, no. 3, pp. 1166-1174, Apr. 2015.

[20] P. J. Shin, P. E. Z. Larson, M. A. Ohliger *et al.*, "Calibrationless parallel imaging reconstruction based on structured low-rank matrix completion," *Magn. Reson. Med.*, vol. 72, no. 4, pp. 959-970, Oct. 2014.

[21] J. Lee, K. H. Jin, and J. C. Ye, "Reference-free single-pass EPI nyquist ghost correction using annihilating filter-based low rank hankel matrix (ALOHA)," *Magn. Reson. Med.*, vol. 76, no. 6, pp. 1775-1789, Dec. 2016.

[22] R. A. Lobos, T. H. Kim, W. S. Hoge, and J. P. Haldar, "Navigator-free EPI ghost correction with structured low-rank matrix models: New theory and methods," *IEEE Trans. Med. Imag.*, vol. 37, no. 11, pp. 2390-2402, Nov. 2018.

[23] J. Lee, Y. Han, J. K. Ryu, J. Y. Park, and J. C. Ye, "K-space deep learning for reference-free EPI ghost correction," *Magn. Reson. Med.*, vol. 82, no. 6, pp. 2299-2313, Dec. 2019.

[24] M. W. Haskell, S. F. Cauley, B. Bilgic *et al.*, "Network accelerated motion estimation and reduction (NAMER): Convolutional neural network guided retrospective motion correction using a separable motion model," *Magn. Reson. Med.*, vol. 82, no. 4, pp. 1452-1461, Oct. 2019.

[25] D. Tamada, M. L. Kromrey, S. Ichikawa, H. Onishi, and U. Motosugi, "Motion artifact reduction using a convolutional neural network for dynamic contrast enhanced MR imaging of the liver," *Magn. Reson. Med. Sci.*, vol. 19, no. 1, pp. 64-76, 2020.

[26] P. M. Johnson, and M. Drangova, "Conditional generative adversarial network for 3D rigid-body motion correction in MRI," *Magn. Reson. Med.*, vol. 82, no. 3, pp. 901-910, Sep. 2019.

[27] B. Duffy, L. Zhao, F. Sepehrband *et al.*, "Retrospective motion artifact correction of structural MRI images using deep learning improves the quality of cortical surface reconstructions," *Neuroimage*, vol. 230, 117756, Apr. 2021.

[28] A. Nachmani, R. Schurr, L. Joskowicz, and A. A. Mezer, "The effect of motion correction interpolation on quantitative T1 mapping with MRI," *Med. Image Anal.*, vol. 52, pp. 119-127, Feb. 2019.

[29] O. Cohen, B. Zhu, and M. S. Rosen, "MR fingerprinting deep reconstruction network (DRONE)," *Magn. Reson. Med.*, vol. 80, no. 3, pp. 885-894, Sep. 2018.

[30] O. Perlman, H. Ito, K. Herz *et al.*, "Quantitative imaging of apoptosis following oncolytic virotherapy by magnetic resonance fingerprinting aided by deep learning," *Nat. Biomed. Eng.*, (Epub 2021 Nov 11), 2021.

[31] L. Chen, M. Schar, K. W. Y. Chan *et al.*, "In vivo imaging of phosphocreatine with artificial neural networks," *Nat. Commun.*, vol. 11, no. 1, pp. 1072, Feb. 2020.

[32] F. Liu, and L. Feng, "k-t SANTIS: subspace augmented neural network with incoherent sampling for dynamic image reconstruction," *in Proceedings of the 28th Annual Meeting of ISMRM Virtual Conference and Exhibition*, 2020, pp. 0998.

[33] F. Liu, R. Kijowski, G. El Fakhri, and L. Feng, "Magnetic resonance parameter mapping using model-guided self-supervised deep learning," *Magn. Reson. Med.*, vol. 85, no. 6, pp. 3211-3226, Jun. 2021.

[34] G. Della Maggiora, C. Castillo-Passi, W. Qiu *et al.*, "DeepSPIO: super paramagnetic iron oxide particle quantification using deep learning in magnetic resonance imaging," *IEEE Trans. Pattern Anal. Mach. Intell.*, vol. 44, no. 1, pp. 143-153, Jan. 2022.

[35] S. Bollmann, K. G. B. Rasmussen, M. Kristensen *et al.*, "DeepQSM - using deep learning to solve the dipole inversion for quantitative susceptibility mapping," *Neuroimage*, vol. 195, pp. 373-383, Jul. 2019.

[36] S. Gavazzi, C. A. T. van den Berg, M. H. F. Savenije *et al.*, "Deep learning-based reconstruction of in vivo pelvis conductivity with a 3D patch-based convolutional neural network trained on simulated MR data," *Magn. Reson. Med.*, vol. 84, no. 5, pp. 2772-2787, Nov. 2020.

[37] P. Liao, J. Zhang, K. Zeng *et al.*, "Referenceless distortion correction of gradient-echo echo-planar imaging under inhomogeneous magnetic fields based on a deep convolutional neural network," *Comput. Biol. Med.*, vol. 100, no. 1, pp. 230-238, Sep. 2018.

[38] J. Tobin, R. Fong, A. Ray, J. Schneider, W. Zaremba, and P. Abbeel, "Domain randomization for transferring deep neural networks from simulation to the real world," *in Proceedings of IEEE International Conference on Intelligent Robots and Systems*, 2017, pp. 23-30.

[39] S. Klein, M. Staring, K. Murphy *et al.*, "elastix: a toolbox for intensity based medical image registration," *IEEE Trans. Med. Imag.*, vol. 29, no. 1, pp. 196-205, Jan. 2010.

[40] H. Gudbjartsson, and S. Patz, "The rician distribution of noisy mri data," *Magn. Reson. Med.*, vol. 34, no. 6, pp. 910-914, Dec. 1995.

[41] S. Li, J. Wu, L. C. Ma, S. H. Cai, and C. B. Cai, "A simultaneous multi-slice T2 mapping framework based on overlapping-echo detachment planar imaging and deep learning reconstruction," *Magn. Reson. Med.*, (Epub 2022 Jan 11), 2022.

[42] M. Uecker, P. Lai, M. M. Lustig *et al.*, "ESPIRiT-An Eigenvalue approach to autocalibrating parallel MRI: Where SENSE meets GRAPPA," *Magn. Reson. Med.*, vol. 71, no. 3, pp. 990-1001, Mar. 2014.

[43] F. Liu, J. V. Velikina, W. F. Block, R. Kijowski, and A. A. Samsonov, "Fast realistic MRI simulations based on generalized multi-pool exchange tissue model," *IEEE Trans. Med. Imag.*, vol. 36, no. 2, pp. 527-537, Feb. 2017.

[44] C. B. Cai, M. J. Lin, Z. Chen, X. Chen, S. H. Cai, and J. H. Zhong, "SPROM - an efficient program for NMR/MRI simulations of inter- and intra-molecular multiple quantum coherences," *C.R.Physique*, vol. 9, no. 1, pp. 119-126, Jan. 2008.

[45] O. Ronneberger, P. Fischer, and T. Brox, "U-Net: Convolutional networks for biomedical image segmentation," *in International Conference on Medical Image Computing and Computer-Assisted Intervention*, 2015, pp. 234-241.

[46] J. Schlemper, J. Caballero, J. V. Hajnal, A. N. Price and D. Rueckert, "A deep cascade of convolutional neural networks for dynamic MR image Reconstruction," *IEEE Trans. Med. Imag.*, vol. 37, no. 2, pp. 491-503, Feb. 2018.

[47] D. O. Walsh, A. F. Gmitro, and M. W. Marcellin, "Adaptive reconstruction of phased array MR imagery," *Magn. Reson. Med.*, vol. 43, no. 5, pp. 682-690, May. 2000.

[48] H. K. Aggarwal, M. P. Mani, and M. Jacob, "MoDL-MUSSELS: Model-based deep learning for multishot sensitivity-encoded diffusion MRI," *IEEE Trans. Med. Imag.*, vol. 39, no. 4, pp. 1268-1277, Apr. 2020.

[49] S. Liu, K. H. Thung, L. Qu *et al.*, "Learning MRI artefact removal with unpaired data," *Nat. Mach. Intell.*, vol. 3, no. 1, pp. 60-67, Jan. 2021.

[50] G. Oh, J. E. Lee and J. C. Ye, "Unpaired MR motion artifact deep learning using outlier-rejecting bootstrap aggregation," *IEEE Trans. Med. Imag.*, vol. 40, no. 11, pp. 3125-3139, Nov. 2021.

[51] A. Sharma, and G. Hamarneh, "Missing MRI pulse sequence synthesis using multi-modal generative adversarial network," *IEEE Trans. Med. Imag.*, vol. 39, no. 4, pp. 1170-1183, Apr. 2020.

[52] M. Yurt, S. U. Dar, A. Erdem, E. Erdem, K. K. Oguz, and T. Cukur, "Mustgan: Multi-stream generative adversarial networks for MR image synthesis," *Med. Image Anal.*, vol. 70, no. 4, pp. 439-448, Feb. 2021.